Chapter 6

MICROANGELO SCULPTING: MICROLENS ARRAY FABRICATION

6.1 Background

In the following two chapters, thermocapillary forces are used to deform molten nanofilms into structures through the spatial modulation of surface tension. We call this technique MicroAngelo (μAngelo) in reference to how it sculpts interface on the microscale. At its most basic level, MicroAngelo operates by modulating thermocapillary forces through the application of a spatially inhomogeneous temperature distribution. As was described in Sec. 2.3.3, thermocapillary forces cause flow from warmer regions of the fluid interface to cooler regions and this induces spontaneous out of plane growth due to random fluctuations in the interface height. By using a patterned mask instead of a flat plate, we can bypass the random nature of instability growth to directly influence the temperature distribution and impose thermal inhomogeneities on the fluid interface which localize the deformation. Two examples of simple masks which create non-uniform temperature profiles are shown in Fig. 6.1. Due to the large disparity between the vertical and lateral length scales, lateral thermal conduction is negligible and so the regions underneath the mask patterns will be colder than the surrounding regions. This drives thermocapillary flow and consequently structure formation in a fabrication technique we call MicroAngelo. In effect, this technique harnesses the physical mechanism behind the instability investigated in the first portion of this thesis to localize and control film growth.

With the maturation of nanofabrication technology, complex optical devices have become increasingly dependent on micro-optical components to shape, filter, and steer light at the microscale. Traditional grinding and polishing techniques are incapable of achieving the fine resolution and optical quality demanded by such applications, thereby necessitating the use of complex multi-step fabrication processes. Conventional photolithography and scanning beam lithography are commonly used and well-established manufacturing processes, but typically require expensive advanced equipment, multiple post-processing steps, and are limited to producing two-dimensional surface structures. Numerous alternative methods of microfabri-

Figure 6.1: Basic MicroAngelo experimental setup for microlens array fabrication

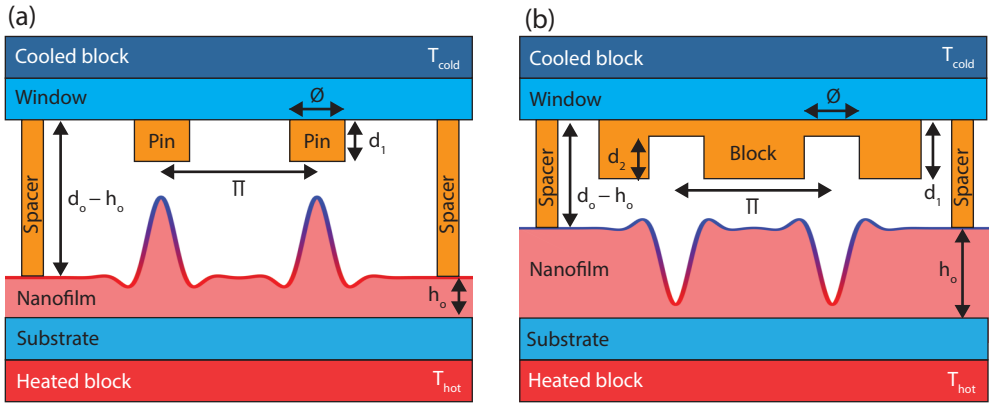

Diagrams of the MicroAngelo setup used to fabricate MLAs. For a full listing of the geometric parameters please consult Table 6.1. (a) Geometry to fabricate convex MLAs. In this configuration, the pins extend from the cooled sapphire window towards the film and growth is localized beneath the pins. (b) Geometry to fabricate concave MLAs. In this configuration, the depressions in the block on the cooled sapphire window localize depressions in the film. The film topographies shown in (a) and (b) are representative late-stage topographies after the film has deformed from its initially flat state. Figure courtesy of Daniel Lim.

cation exist to circumvent these challenges. Hou *et al.* detail twelve categories of fabrication procedures just to fabricate microlens arrays (MLAs) [55], the archetypal micro-optical device comprising periodically spaced micro-lenses arranged on a two-dimensional plane.

While the production of microlens arrays has a long history [56], the fabrication of microlens arrays with thermocapillary forces is quite minimal. Previously in the Troian group, Dr. Euan McLeod produced lens-like structures on silicon wafers using a mask design similar to Fig. 6.1(a) [16]. After Euan left the group, additional lens arrays on silicon wafers were fabricated, as seen in Fig. 6.2. While these arrays showed strong ordering, they were not functional as transmissive, refractive optical devices. When Daniel Lim started working in the lab, we wanted to do a comprehensive study of this fabrication process to explore the range of possible topographies, as well as transition from an opaque substrate (silicon) to a transparent one (fused quartz) so that the devices could be used in transmission like conventional microlens arrays.

The remainder of this chapter is organized as follows. First, we examine the experimental setup and detail the fabrication procedure with MicroAngelo in Sec. 6.2. Then, we describe the characterization of the microlens arrays in Sec. 6.3. After that, we discuss numerical simulations of the lens evolution process in Sec. 6.4. Next,

Figure 6.2: Optical images of MLAs produced on silicon wafers

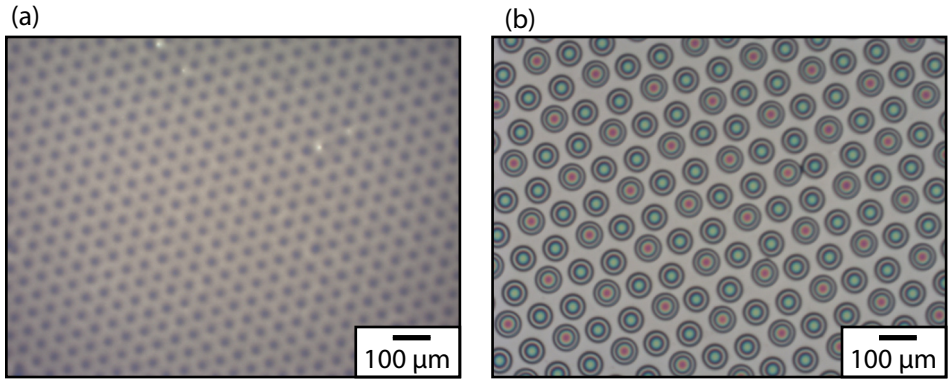

Optical microscope images of microlens arrays fabricated on silicon which show strong ordering. The colors are due to thin film interference fringes and reflect the film height similar to topographic maps. The lenses in (a) are small in height and do not show a full fringe and appear as dark spots. In (b), there are two different lens heights, as evidenced by the different colors of the lens apices.

we implemented a Shack-Hartmann wavefront sensor using an MLA fabricated with MicroAngelo in Sec. 6.5. Finally, we conclude with a discussion of the fabrication results in Sec. 6.6 and a brief summary in Sec. 6.7.

6.2 Experimental Setup and Fabrication Procedure

The experimental setup used for micro-optical device fabrication in this chapter and the next is conceptually very similar to the setups used for the flat plate experiments presented in Ch. 3, Ch. 4, and Ch. 5. However, there are several key differences and improvements which will be detailed below.

As shown in Fig. 6.3, a polymer nanofilm is heated from below and actively cooled from above in the presence of a photoresist pattern which localizes the temperature gradient and heat flux to produce the desired optical structures. Starting from the bottom of the setup and working upwards, the heating assembly and PS nanofilm were supported by a spring-mounted riser plate on a motorized z-translation stage (Oriel 16618). The springs allowed small deflections in tip and tilt of the heater so that the nanofilm and its supporting wafer would be parallel to the sapphire window. The heater was isolated thermally from the rest of the setup using fiberglass insulation. The ceramic heating element (Induceramic, 5.2 Ω, 25.4 mm square) was enclosed in a custom fabricated aluminum holder (50.8 mm diameter cylinder) and was powered by a DC power supply (Keithley 2200-30-5). Three holes were drilled into the aluminum holder for platinum RTDs (Omega RTD-3-F3105-36-T) which were monitored continuously by a data acquisition module attached to a computer

(Omega PT-104A). The RTD holes were located at the center of the holder, halfway to the edge, and at the edge of the holder. This holder was superior to the holder described in Sec. 5.2 because it was smaller and matched the size of the substrates better. Consequently, it localized heat flux more effectively through the nanofilm and its substrate. The measured temperature of the middle RTD (T_{Hot}) was controlled through active PID feedback in a custom MATLAB GUI controller. A small amount of thermal paste (Aremco Heat-Away 638, approximately 150 mg, 130 μm thick cylindrical layer) was used to ensure good thermal contact between the aluminum heater holder and the fused quartz windows (Ted Pella 16001-1, 25.4 mm diameter, 1.6 mm thickness) which served as the PS substrate.

To create the nanofilm, the PS (Scientific Polymer Products, M_w = 1100, M_n = 990) was dissolved in toluene, filtered, and then spun-coat onto the polished quartz substrates or silicon wafers (Silicon Materials, 50.8 mm diameter, <100> orientation, 279 ± 25 μm thickness). The film thickness of the PS on quartz was inferred from ellipsometry measurements of the same solution spun onto the silicon wafers which were measured using ellipsometry (Rudolph Auto EL III). We attempted to measure the PS thickness on the fused quartz directly but found that the index contrast between the two materials (n_{PS} = 1.58 vs. n_{Ox} = 1.457 at a wavelength of 632.8 nm) was too small to produce a reliable signal. There were also additional complications from back reflections off the back of the fused quartz substrate. Film thicknesses were averaged over nine measurements of a 3×3 grid near the center of the silicon wafer at 632.8 nm. The top of the PS nanofilm was contacted by the photoresist spacers (MicroChem SU-8 2010) which were photolithographically patterned on sapphire windows (Meller Optics MSW 037/040). The cylindrical spacers were arranged hexagonally at a radius of 3 mm and had heights ranging from 1.3 μm to 1.8 μm with a diameter of 1000 μm. An additional photoresist pattern was deposited in the center of the sapphire window which served to define the microlens array pattern and morphology. The patterns were generally on the order of 700 nm to 900 nm and a full listing of the geometric parameters can be found in Table 6.1. The photoresist spacers and patterns were cured using UV light (Karl Suss MJB3) through a custom chrome-on-glass patterned mask (UCLA Nanolab Mask Shop). After UV curing, the photoresist was hard baked at 200 °C for 2 hours to stabilize the structures. Then a self-assembled monolayer of perfluorooctyltrichlorosilane (PFOTS, Sigma Aldrich, CAS #78560-45-9) was deposited on the windows through molecular vapor deposition in an evacuated dessicator. The spacer and pattern heights were measured using stylus profilometry (Ambios XP2). Prior to use (either

spin coating or photolithrography), both the fused quartz and sapphire disks were cleaned using piranha (3:1 stock sulfuric acid to 30% hydrogen peroxide) to remove any organic contamination. The disks were placed in the solution for at least 15 minutes. After removal from the piranha solution, the windows were immediately rinsed in deionized water (Milli-Q Gradient A10). They were then rinsed in acetone and dried with nitrogen.

The silanized windows were placed directly on top of the solid polymer nanofilm before heating began and were brought into physical contact with the upper aluminum chiller. The custom machined chiller was water-cooled using an external thermal reservoir (Fisher Scientific Model 910). The other major improvement that this setup had as compared to the one presented in Ch. 5 is that there was no viewing hole in the aluminum chiller block for visualization making the convention of calling it a "window" inaccurate. However, to preserve consistency with previous chapters we will continue to refer to them as windows. The absence of this hole meant that while the growth could not be measured *in situ*, the driving thermal fields were much more uniform. The increased uniformity of the temperature field meant a corresponding increase in the uniformity of the fabricated structures. After insertion into the setup, the heater was engaged and temperature of the center RTD reached the desired setpoint to within ±1 °C in a time of approximately 5 minutes. After a predetermined length of time ranging from 5 minutes to 120 minutes, the ceramic heating element was automatically turned off and the setup allowed to cool. The setup cooled to within 10 °C of the cold reservoir temperature (measured with the center RTD) before the sample was removed.

6.3 Microlens Array Characterization

The characterization of the microlens arrays produced by thermocapillary replication began with inspection of the surface profile using coherence scanning interferometry (also called scanning white light interferometry). In this technique, white light incident on the sample surface is interfered with light which passed through a reference arm. The resulting interference pattern shows fringes modulated by an overall Gaussian envelope. The maximum of the envelope occurs when the length of the reference arm equals the length of the sample arm, so from this measurement the surface profile of the sample can be measured. Using a Zygo NewView 600 and a Zemetrics Zegage, we measured the surface profile of the fabricated microlens arrays and have presented four qualitatively distinct topologies in Fig. 6.4. The full list of fabrication parameters can be found in Table 6.1.

Figure 6.3: Diagram of the full MicroAngelo experimental setup

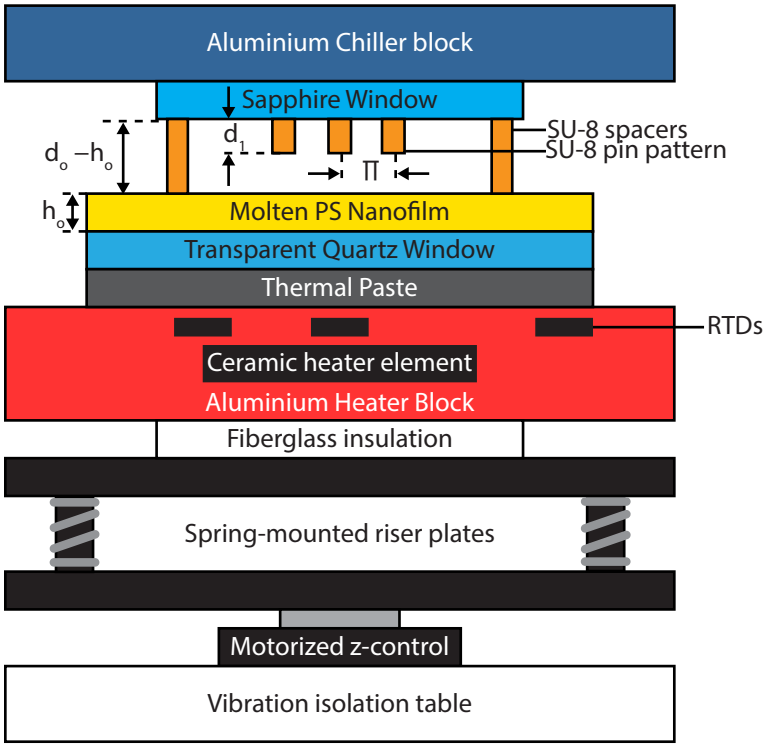

Diagram of the experimental setup used for MicroAngelo fabrication. Consistent with the geometries defined in previous chapters, the sample is heated from below and actively cooled from above. A full listing of the dimensions and parameters can be found in the text and in Table 6.1. Figure courtesy of Daniel Lim.

Fig. 6.4 exhibits four representative MLA topographies achieved through MicroAngelo fabrication, imaged using coherence scanning interferometry. The fabrication parameters and surface characteristics for each of the topographies are listed in Table 6.1. As seen in Fig. 6.4(a) and (b), we have successfully achieved both convex (converging) and concave (diverging) MLAs. Simple topologies are formed when the pin diameter, D_p, is much larger than the center-to-center pattern pitch, Π. When D_p is around the size of Π, the concave ridges around convex microlenses overlap to form smaller interstitial lens arrays. This achieves a hierarchical MLA structure where a smaller array of lenses is formed in the interstitial region of the larger lens array, as seen in Fig. 6.4(c). Hierarchical MLAs exhibit two distinct length scales, corresponding to the vertical size of the two lens arrays. We also report the fabrication of a lens structure with a central depression at the vertex of each microlens, seen in Fig. 6.4(d), which we call the caldera-like structure. During the course of this project, we discovered that the caldera-like microlens structure bears a strong resemblance to the microdonut topology fabricated by Vespini *et al.*

Figure 6.4: Topographies of fabricated microlens arrays

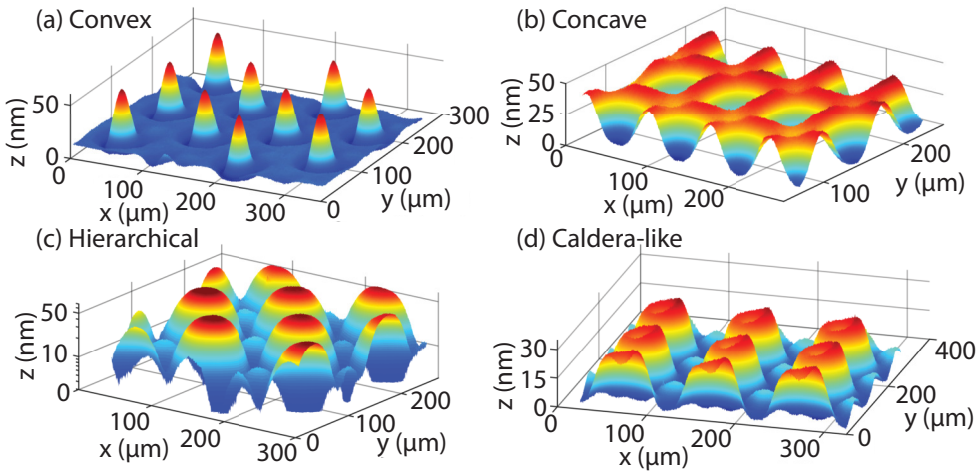

Surface topographies of fabricated microlens arrays imaged using coherence scanning interferometry. Note that the vertical axes have units of nanometers and the horizontal axes have units of microns; all microlenses shown here are actually wide and shallow. (a) Convex microlens array composed of converging lenses. (b) Concave microlens array composed of diverging lenses. (c) Hierarchical microlens array formed from two interdigitated arrays of different sizes. The vertical scale is logarithmically plotted to highlight the shorter secondary array between the main peaks. (d) Caldera-like microlens array with a central depression at the vertex of each lens. An additional array of smaller lenses is also visible in the interstitial region. Figure courtesy of Daniel Lim.

through spin-coating polymer onto a patterned pyroelectric substrate [57]. While Vespini *et al.* attributes the central depression formation to a slump of material away from the protrusion vertex during spin-coating, we will show through first-principles computational simulation in Sec. 6.4 that our caldera-like arrays evolve from the bottom-up and outside-in. The technique investigated by Vespini *et al.* has only achieved convex caldera-like ("microdonut") structures, whereas MicroAngelo has achieved concave caldera-like topologies as well and hence has access to a larger variety of curved topologies.

Beyond the qualitative observations gleaned from observation of microlens array surface profiles, we have also quantitatively characterized the microlens array properties using this surface profile data. In particular, we measured the lens diameter, fill factor, focal length, Fresnel number, asphericity, and surface roughness. Each of these measurements will be examined in the following sections.

6.3.1 Lens Diameter and Fill Factor

Since the lenses are formed with a continuous surface profile, there is no clear delineation between a lens and the neighboring interstitial regions. We defined a

Table 6.1: Parameter values for the fabricated microlens arrays

	Convex	Concave	Hierarchical	Caldera-like
t (min)	30	60	15	45
T_{cold} (°C)	60	60	60	60
T_{hot} (°C)	180	180	180	180
$d_o - h_o$ (nm)	1630 ± 40	1430 ± 50	1400 ± 30	1410 ± 20
d_1 (nm)	805 ± 7	880 ± 10	730 ± 10	730 ± 10
d_2 (nm)	-	320 ± 20	-	-
D_p (μm)	20	50	50	50
Π (μm)	100	75	100	100
h_o (nm)	228 ± 2	288 ± 4	288 ± 4	288 ± 4

Parameter values for the four microlens arrays imaged in Fig. 6.4. Uncertainties are one standard deviation unless otherwise stated. t is the fabrication time for which the heating elements were active. d_2 is the depth of the photoresist depression in a block and is only applicable to concave microlens array fabrication, as in the experimental setup shown in Fig. 6.1(b).

lens as the region of all contiguous pixels of the same curvature. Note that for the caldera-like lenses we included the center region of opposite curvature. We chose to use 8-connected pixels to determine neighboring pixels. The calculation of mean curvature is very noisy when performed on raw interferometric data, so first we smoothed the raw data using a cubic smoothing spline in MATLAB [25] (csaps routine with smoothing parameter set to 10^{-4}). From the fitted cubic spline, the mean curvature at all points was calculated and the points with the appropriate curvature were grouped together to form a lens. Note that the cubic spline was only used to find the points which were part of the lens. All calculations and derived values were performed on the raw and unsmoothed interferometric data. Since the resulting region was not strictly circular, we defined a characteristic diameter of the lens, D_{lens}, from the total area of the lens, A_{lens}, by the relation

$$D_{\text{lens}} = 2\sqrt{\frac{A_{\text{lens}}}{\pi}}. \tag{6.1}$$

The fill factor of the lens array was calculated by taking A_{lens} and dividing by the area of a unit cell. The computed lens diameters and fill factors can be found in Table 6.2.

6.3.2 Focal Length and Fresnel Number

With the lens domain determined by the sign of the curvature, the focal lengths of the fabricated microlenses were estimated by fitting the raw data within the lens domain to a paraboloid of the form

$$z(x, y) = z_{max} - \frac{(x')^2}{2R_1} - \frac{(y')^2}{2R_2}, \tag{6.2}$$

where z_{max} is the height of the lens at its vertex and R_1 and R_2 are the radii of curvature along the lateral principal axes, x' and y'. The principal axes of the lens are not guaranteed to coincide with the native coordinate system (x and y) of the interferometry data, so we used rotated coordinates

$$\begin{pmatrix} x' \\ y' \end{pmatrix} = \begin{pmatrix} \cos\theta & -\sin\theta \\ \sin\theta & \cos\theta \end{pmatrix} \begin{pmatrix} x - x_o \\ y - y_o \end{pmatrix}, \tag{6.3}$$

where θ is the angle of rotation of the principal axes (x', y') to the raw data axes (x, y) and (x_o, y_o) are the coordinates of the lens vertex in the raw data coordinates. The use of two independent radii of curvature allows us to account for any astigmatism in the lens. The corresponding focal lengths, f_1 and f_2, are then calculated from the lensmaker's equation using R_1 and R_2

$$\frac{1}{f_i} = \frac{n - 1}{R_i}, \tag{6.4}$$

where we have assumed that the lens is thin and that the back side of the lens is planar, corresponding to an infinite radius of curvature. The larger of the two calculated focal lengths was defined to be f_1 and the smaller was defined to be f_2. Since these lenses were used with HeNe lasers with an optical wavelength of 632.8 nm, a refractive index of 1.580 was used for the PS. This value was measured in our lab using an Abbe refractometer; for more details on this instrument please see Appendix A.6.

With the calculated lens diameters and focal lengths, we can evaluate whether the lenses are operating in the near-field or far-field regime at the focal plane of the MLA using the Fresnel number. The Fresnel number, evaluated at the focal plane of the lens, is defined by

$$F = \frac{a^2}{\lambda_{\text{opt}} f}, \tag{6.5}$$

where a is a characteristic size of the aperture and λ_{opt} is the wavelength of light at which the lens is being used. If F is less than 1, the beam is in the far-field while if F is greater than 1, the beam is in the near-field. In our case, we can evaluate the Fresnel numbers for both individual lenses, F_{lens}, and for the whole array F_{array}. These expressions are

$$F_{\text{lens}} = \frac{D_{\text{lens}}^2}{4\lambda_{\text{opt}} f}, \tag{6.6}$$

$$F_{\text{array}} = \frac{\Pi^2}{\lambda_{\text{opt}} f}, \tag{6.7}$$

where Π is the spatial period of the array. In all cases, the Fresnel numbers are small compared to unity, as can be seen in Table 6.2. This means that the lenses are operating in the Fraunhofer regime at the focal plane and diffraction is important.

6.3.3 Asphericity and Surface Roughness

To justify the selection of a paraboloidal geometry over a spherical geometry and quantify the degree of asphericity, we fit the lens cross section along its principal axes to an aspheric profile of the form

$$z(r) = z_{\text{max}} - \left[\frac{r^2}{(D_{\text{lens}}/2)\left(1 + \sqrt{1 - r^2/(D_{\text{lens}}/2)^2}\right)} + \alpha_4 r^4 \right], \tag{6.8}$$

where α_4 is the first aspheric coefficient and quantifies the degree of asphericity. The larger the value of α_4, the less spherical is the 1D lens profile. The lens profiles are displaced vertically so that the minimum (maximum) of the fitted convex (concave) lens lies at zero height and z_{max} corresponds to the height of the lens. To allow comparison of this asphericity over different lens sizes, we defined the asphericity ratio as the ratio of the α_4 contribution to the surface profile relative to the lens height, evaluated one characteristic radius away from the lens vertex

$$\text{AR} \equiv \left| \frac{\alpha_4 (D_{\text{lens}}/2)^4}{z_{\text{max}}} \right|. \tag{6.9}$$

The AR values calculated for the MLAs in Table 6.2 are less than one but still on the order of unity, indicating that the contribution due to the perturbing polynomial

is comparable to that of the spherical geometry. This result corroborates with the excellent fits obtained by the 2D paraboloidal surface in Eq. (6.2) over the lens surface. As a point of comparison for these reported values, a commercial spherical microlens array (Thorlabs MLA150-5C-M) evaluated using the same process yields an AR value of 0.04 ± 0.03 and a commercial parabolic microlens array (Thorlabs MLA300-14AR-M) yields a larger AR value of 0.13 ± 0.02.

The root mean square (RMS) residual of the 2D surface fit has two main contributions: the non-conformity of the microlens geometry to the paraboloid shape and the high spatial frequency surface roughness contribution. The RMS residual of this fit therefore provides an upper bound to the surface roughness of the fabricated surfaces. The majority of the microlens fits achieve an RMS residual of less than 2 nm, which also provides an upper bound to the low surface roughness of the ultrasmooth microlenses.

6.4 Numerical Simulations of Lens Evolution

To numerically simulate the growth and evolution of a microlens as a function of time, we have to return to the thin film equation for the thermocapillary model which was derived in Sec. 2.3.3. Specifically, we need a generalized form of Eq. (2.106) because that equation was derived under the assumption of perfectly flat, infinite bounding plates. Now that the top plate has nontrivial topography, we replace the constant D with a variable expression, $G(x, y)$, which describes the mask topography. The derivation proceeds identically to that presented in Ch. 2. The difference is that when we take the surface gradient of Γ the surface gradient acts on the variable G. G then replaces D in the denominator of the nondimensional temperature. As such, the thin film evolution equation for the TC model in the presence of bounding plates with topography is

$$\frac{\partial H}{\partial \tau} + \widetilde{\boldsymbol{\nabla}}_{||} \cdot \left[\frac{H^3}{3\overline{Ca}} \left(\widetilde{\boldsymbol{\nabla}}_{||}^3 H \right) + \frac{H^2 \kappa \overline{Ma}}{2} \widetilde{\boldsymbol{\nabla}}_{||} \left(\frac{H}{G + (\kappa - 1)H} \right) \right] = 0. \tag{6.10}$$

As before, H is the dimensionless film thickness, G is the dimensionless mask topography, τ is the dimensionless time, $\overline{Ca}$ is the modified capillary number, $\overline{Ma}$ is the modified Marangoni number, and κ is the thermal conductivity ratio. To proceed further with the finite element simulations this equation must be rewritten in terms of a coupled set of differential equations whose highest order derivatives are only

Table 6.2: Measured and derived values of the fabricated microlens arrays

	Convex	Concave	Hierarchical (interstitial array)	Caldera-like (depression)
D_{lens}	29.4 ± 0.5	51.3 ± 0.6	71 ± 2	71.0 ± 0.4
(μm)			(30 ± 2)	(21.6 ± 0.8)
Fill factor	7.9 ± 0.3	36.7 ± 0.8	39 ± 2	39.6 ± 0.4
(%)			(7.2 ± 0.7)	(3.7 ± 0.3)
f_1	6.2 ± 0.7	−23 ± 2	38 ± 9	
(mm)			(70 ± 10)	(−34 ± 6)
f_2	5.4 ± 0.3	−22 ± 2	29 ± 7	
(mm)			(47 ± 7)	(−23 ± 3)
$F_{\text{lens}} \times 10^{3\dagger}$	59 ± 5	46 ± 4	63 ± 14	
			(7 ± 2)	(7 ± 2)
$F_{\text{array}} \times 10^{3\dagger}$	687 ± 67	98 ± 8	127 ± 31	
			(72 ± 4)	(148 ± 36)
AR	0.5 ± 0.2	0.12 ± 0.03	0.5 ± 0.5	
			(0.5 ± 0.3)	(0.4 ± 0.2)
Roughness	1.3 ± 0.5	0.7 ± 0.1	1.4 ± 0.6	
(nm)			(0.49 ± 0.04)	(0.44 ± 0.02)

MLA parameters were measured for at least 10 lenses randomly selected over the array. Uncertainties are one standard deviation unless otherwise stated. For the hierarchical and caldera-like arrays, the values reported within parentheses correspond to the interstitial array and the central depression, respectively, while the main array values are immediately above them.
†Parameter was calculated at the HeNe laser wavelength λ_{opt} = 632.8 nm.

of second order. This yields

$$\frac{\partial}{\partial\tau}\begin{bmatrix} H \\ 0 \end{bmatrix} + \widetilde{\boldsymbol{\nabla}}_{||} \cdot \begin{bmatrix} \dfrac{1}{3\overline{Ca}} H^3 \widetilde{\boldsymbol{\nabla}}_{||} C + \dfrac{\kappa\overline{Ma}}{2} \dfrac{GH^2}{[G+(\kappa-1)H]^2} \widetilde{\boldsymbol{\nabla}}_{||} H \\ \widetilde{\boldsymbol{\nabla}}_{||} H \end{bmatrix} - \widetilde{\boldsymbol{\nabla}}_{||} \cdot \begin{bmatrix} \dfrac{\kappa\overline{Ma}}{2} \dfrac{H^3}{[G+(\kappa-1)H]^2} \widetilde{\boldsymbol{\nabla}}_{||} G \\ \widetilde{\boldsymbol{\nabla}}_{||} H \end{bmatrix} = \begin{bmatrix} 0 \\ C \end{bmatrix}, \quad (6.11)$$

where C is a dummy variable which equals the Laplacian of the film height, H. Within the context of these simulations, there is a well-defined lateral length scale,

the mask pin pitch, Π. As such, the same expressions from Ch. 2 still hold, but with L replaced by Π. This equation is now suitable for simulation in the commercial finite element simulation program, COMSOL [28]. The constituent elements are P2 Lagrange triangular elements.

The specific geometry chosen for the simulations is diagrammed in Fig. 6.5. A set of four pins arranged in a 2x2 grid were suspended over a nanofilm and the domain was modeled using periodic boundary conditions on all the lateral boundaries. Note that in the dimensionless units chosen for the simulations, the film thickness was 1 vertical unit and the mask pin pitch was also 1 lateral unit. The specific G that describes this geometry is

$$G = \frac{d_o}{h_o}(1 - \delta \times f_p), \tag{6.12}$$

where $\delta = d_1/d_o$ and f_p is the protrusion function which is a periodic extension of COMSOL's built-in rectangle function over the [0,2]×[0,2] computational domain.

$$f_p(x, y) = \text{rect}\left[\sqrt{(x - 0.5)^2 + (y - 0.5)^2}\right]. \tag{6.13}$$

The rectangle function was set to have an upper limit of 0.25 and a lower limit of -0.25 and a transition zone width of 0.1. The initial condition for the simulation was a dimensionless film height of unity plus small random noise

$$H(x, y, \tau = 0) = 1 + 0.1 \times rn(x, y), \tag{6.14}$$

where $rn(x, y)$ is the 2D random number generator native to COMSOL. Each argument of the random function is sampled from a normal distribution with $\mu = 0$ and $\sigma = 0.05$. Note that the model is not sensitive to the random initial height because the capillary term in the the thin film equation damps out high spatial frequency components and the time-dependent COMSOL computation is based on an implicit backward differentiation solver. These two facts guarantee the numerical stability of the solution and eliminate the high frequency components after the first timestep.

To further investigate the formation dynamics of the caldera-like MLA presented in Fig. 6.4(d), we chose the same parameters for the numerical system as were used in the experimental fabrication. A full listing of the parameters used in the simulation can be found in Table 6.3. We note that the temperature drop ΔT was computed from

Figure 6.5: Geometry of the mask used in MLA finite element simulations

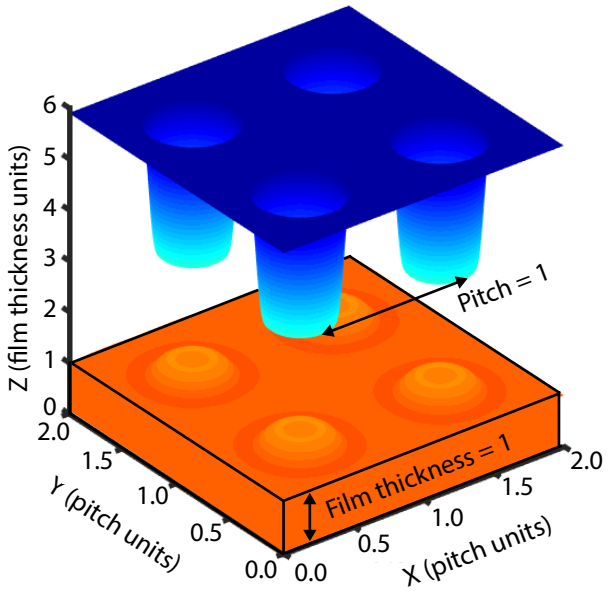

COMSOL simulation geometry of a 2x2 array of pins (blue) above a molten polymer surface (orange). Vertical heights are normalized to the initial film thickness and horizontal lengths are normalized to the pitch of the periodic array. Figure courtesy of Chengzhe Zhou.

a separate steady state finite element simulation of the temperature in the domain, consistent with the simulations described in Sec. 5.3.

The results of the finite element simulations described by Table 6.3 are shown in Fig. 6.6. Fig. 6.6(a) contains cross sections from the experimental surface profile measurements of Fig. 6.4 for comparison. Looking at the cross sections of the numerical simulations in Fig. 6.6(b) we see that polymer begins accumulating below the edges of the chilled pins to form a ring-like protrusion (0.6 minutes), then forms a caldera-like lens with a wide central depression (4.5 minutes). At late times, the central depression vanishes (5.7 minutes) and the microlenses form convex topographies (6.5 minutes). This transition from a caldera-like topography to a convex topography is also shown in Fig. 6.6(c) where the height of the central point in the microlens and the highest point of the microlens are simultaneously plotted. As we see, the caldera-like topographies are a transitory early stage in the film evolution and can only be accessed by halting fabrication during a specific regime.

6.5 Microlens Array Application: Shack-Hartmann Wavefront Sensor

To further characterize the MLAs fabricated with MicroAngelo, we wanted to investigate the focusing behavior of the caldera-like lenses as well as use them in a

Table 6.3: List of parameters for the simulation of microlens evolution

Parameter	Description	Value
h_o	Unperturbed film height	288 nm
$d_o - h_o$	Spacer height	1410 nm
d_1	Pin height	730 nm
Π	Pin pitch	100 μm
D_p	Pin diameter	50 μm
ΔT	Temperature jump across gap	6.27 K
γ	Film surface tension (extrapolated) [22]	3.5×10^{-2} N/m
$-d\gamma/d$T	Surface tension temperature coefficient [22]	7.2×10^{-5} N/(m-K)
k_{air}	Air thermal conductivity (interpolated) [21]	0.032 W/(m-K)
k_{film}	Film thermal conductivity [22]	0.128 W/(m-K)
η	Film viscosity (interpolated) [24]	32.5 Pa·s
ϵ	h_o/Π	0.00288
$\overline{CaMa}$	$\frac{\cancel{\eta\mu_c}}{\gamma\epsilon^3}\frac{\epsilon\gamma_{\text{T}}\Delta\text{T}}{\cancel{\eta\mu_c}}$	1490
D	$\frac{d_o}{h_o}$	5.90
δ	$\frac{d_1}{d_o}$	0.430
κ	$k_{\text{air}}/k_{\text{film}}$	0.247
t_{viscous}	$\eta\Pi/\gamma\epsilon^3$	3.89×10^6 s

Shack-Hartmann wavefront sensor. Shack-Hartmann wavefront sensors are devices which measure wavefront distortion and have applications in adaptive optics [58]. The general premise of this type of sensor is that each lens in the array will focus an incoming plane wave to a distinct spot on a camera. If the incoming plane wave has been perturbed, then the location of the focused spot will shift on the camera and this can be used to determine properties of the incident wave. A diagram of our implementation of a SHWS is shown in Fig. 6.7. In this setup we spatially filtered the output of a 632.8 nm HeNe laser, collimated the resulting beam and transmitted it through an MLA where it was then imaged. The air perturbations were then introduced between the collimating lens and the MLA.

Before we get to the results of the SHWS setup, we wanted to verify that our lenses adequately focused light and to probe the transmission pattern of the caldera-like

Figure 6.6: Comparison of experimental MLA cross sections to numerical simulation cross sections

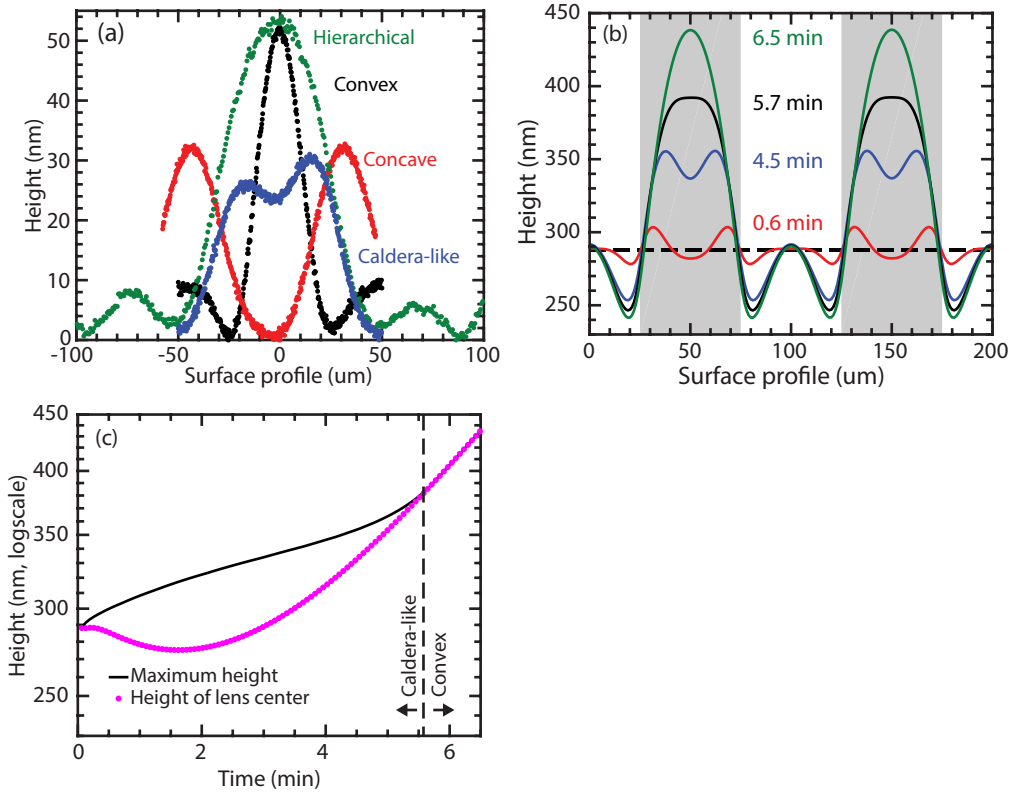

(a) Experimental cross sections from coherence scanning interferometry of microlenses from each of the four arrays in Fig. 6.4. (b) Cross sections from the simulation of convex microlens array evolution at four times. The gray shaded region represents the points directly under the photoresist pins. (c) Time dependence of the maximum height of a single microlens and central height of the microlens. The central region is initially lower than the maximum height, indicating that the microlens formed a caldera-like geometry with a concave top. At late times the central region becomes the highest point, indicating a transition from a caldera-like regime to a convex regime. Figure courtesy of Chengzhe Zhou and Daniel Lim.

lenses. The radial intensity of the transmitted light through a caldera-like MLA as a function of displacement from the lens surface is shown in Fig. 6.8(a). In this figure we see a clear annular focus at the left dashed line (green) and the corresponding camera image is shown in Fig. 6.8(b). Further away from the surface of the lens, at the right dashed line (red), we see that the light has been focused to an approximately Gaussian spot in Fig. 6.8(c). The central depression has opposite curvature and is responsible for the initial annular focusing. Further away, the MLA behaves as an ordinary converging lens array would. This data was recorded by placing the MLAs lens-side up on an optical microscope (Olympus BX60 with Olympus UMPlanFL 5x, 0.15 NA, 20.0 mm working distance objective) configured

Figure 6.7: Diagram of the Shack-Hartmann wavefront sensor setup

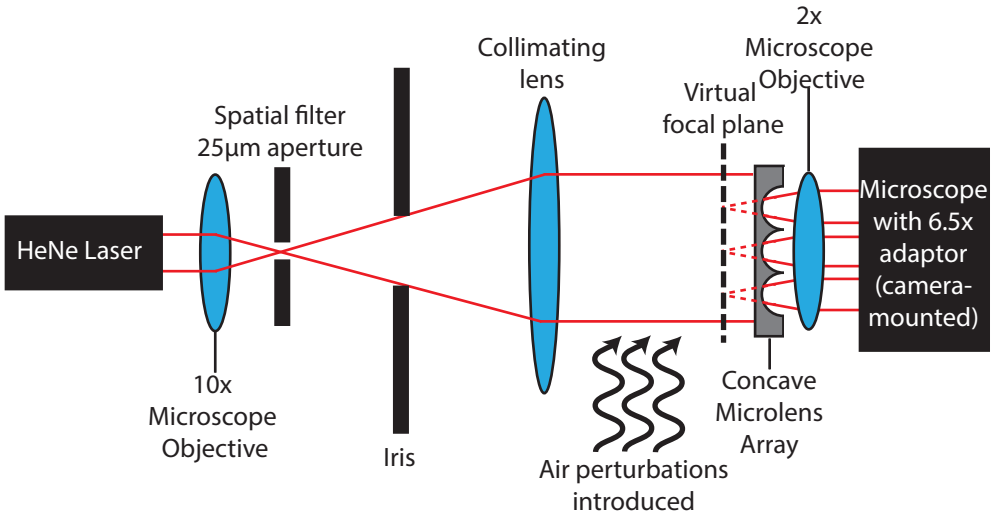

Shack-Hartmann wavefront sensor experimental setup for evaluating concave microlens arrays. Air perturbations will displace the incoming wavefront which is imaged by the MLA and the camera. Figure courtesy of Daniel Lim.

for transmitted light illumination from a halogen bulb. The vertical position of the MLAs was controlled to an accuracy of 1 μm using the microscope fine adjust knob and the resulting transmitted light images were captured at various vertical distances using a high resolution monochrome CMOS camera (Basler acA2500-14gm, 2592 $\times$ 1944 pixels, 2.2 μm $\times$ 2.2 μm pixel size) with a fixed exposure time set to avoid pixel saturation at any pixel in the stack. The zero of the vertical displacement was taken to be at the position where the surfaces of the lenses were in focus. The images were aligned in ImageJ (Template matching and Slice alignment plugin) [59–61] and were imported into MATLAB for radial averaging of the pixel intensities to be performed around each lens focus position. The radial averaged intensity distributions for each of 53 lens positions were averaged to obtain the radial intensity distribution for a single cross-sectional slice.

The remainder of Fig. 6.8 shows the results of a caldera-like MLA in a SHWS. This MLA had very large concave depressions that effectively behaved like a diverging MLA. This implementation of a SHWS is different than conventional approaches, which typically use converging lens arrays [58]. In our modified SHWS, a Helium-Neon laser (λ_{opt} = 632.8 nm, 05-LHP-991, Melles-Griot) was attenuated (ND 1.5, 30898, Edmund Optics), focused through a microscope objective (10x, 0.25 NA, Newport) onto a spatial filter (25 m diameter, 910PH-25, Newport) and collimated (KPX115AR.14 plano-convex lens, Newport). An iris was used to transmit only the

central Gaussian spot to be normally incident on the planar face of the fused quartz MLA substrate. A caldera-like MLA was used in conjunction with a 2x microscope objective (Mitutoyo M Plan Apo 2, NA 0.055, working distance 34 mm) to focus the incident wavefront onto a dot array. The microscope objective was coupled to a high resolution monochrome CMOS camera (Basler acA2500-14gm, 2592×1944 pixels, $2.2\ \mu\text{m} \times 2.2\ \mu\text{m}$ pixel size) by a Navitar 6.5x ultra-zoom lens. The microlens array was mounted onto a micrometer translation stage oriented along the direction of laser propagation and was positioned in front of the virtual focal plane so that the camera recorded an array of focused laser dots. The air in between the collimating lens and the microlens array was perturbed using short sprays of a canned air duster (Miller-Stephenson MS-222N containing 1,1,1,2- Tetrafluoroethane). The duster sprays were oriented perpendicular to the optical axis to avoid physical movement of the optical components. Since the shifts in dot array position were minuscule, the recorded video of the focused dots evolving under the air perturbation was processed using ImageJ in two steps. Firstly, an image of the dot array positions under stationary experimental conditions was subtracted from each frame in the video to accentuate the spatial displacement of each focused beam. Only focused dots that were displaced from their equilibrium positions were visible after this step. Secondly, the subtracted images were thresholded at the same level and converted into binary masks for improved contrast. Fig. 6.8(d) is an example of the perturbed dots after they have been processed, showing the location of the air perturbation. In Fig. 6.8(e) you can see the regular array of focused spots when there is no perturbation in the system which is subtracted from each video frame.

6.6 Discussion of Microlens Fabrication with MicroAngelo

As we presented the fabrication of microlenses in this chapter, there are several salient features of this process to highlight. First, since MicroAngelo is a noncontact technique, the fabricated microlens surfaces are very smooth, as was verified through the use of coherent scanning interferometry data. Surface roughness on the order of 2 nm corresponds to less than a 1% variation in total lens thickness. Beyond the quality of the fabricated lenses, MicroAngelo is a parallel fabrication technique able to make lens arrays over a large area. The MLAs presented above are approximately 2 mm square and this can easily be increased by using a large mask pattern. The only limit on the lateral extent of the fabricated arrays is a practical concern raised by the difficulty of keeping two flat plates parallel at a separation distance of a micron over large lateral distances. Additionally, we have demonstrated that MicroAngelo

Figure 6.8: Caldera-like MLA transmitted light profiles and SHWS image

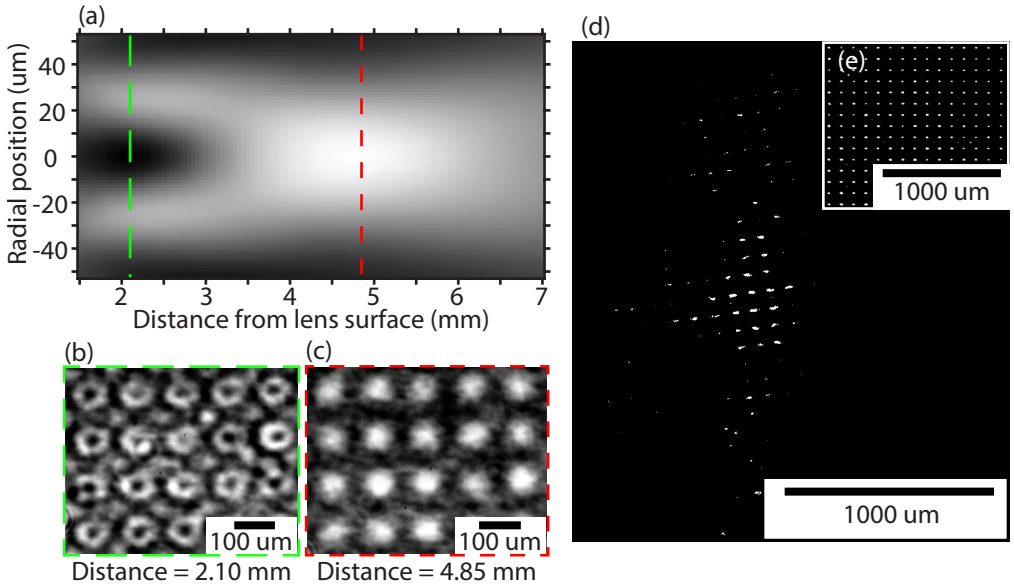

(a) Radial intensity of transmitted light through caldera-like array lens shown in Fig. 6.4(d) as a function of vertical displacement from the lens surface. The plot is azimuthally symmetric about the optical axis (radial position zero). (b) Transmitted light image captured 2.10 mm from the surface of the caldera-like MLA, corresponding to the green dotted line position in (a). Annular focusing with a central minima is observed due to the central caldera lens depression. (c) Transmitted light image captured 4.85 mm from the surface of the caldera-like MLA, corresponding to the red dashed line position in (a). Approximately Gaussian focusing is observed due to the convex portion of the lens. (d-e) Focused dot arrays from a collimated light source transmitted through a concave microlens array. Scale bars refer to distances along the camera sensor. The images have been despeckled once and the contrast has been enhanced. (d) Still frame of an air disturbance proceeding from left to right. The visible dots indicate positions where the focused dot was displaced from the still-air position. (e) The dot array in still air is well-defined and highly regular. Figure courtesy of Daniel Lim.

is capable of producing a variety of unique lens topographies from a single mask pattern by freezing the film at a transitory state in the film evolution process. This means that with suitable control of the process parameters exotic geometries can be achieved, such as the caldera-like lens arrays, which would not be accessible using a fabrication technique that always came to equilibrium.

While we believe that MicroAngelo has great potential for fabrication of micro-optical components, there are a couple areas where improvement is necessary. First, in the above work we were not able to achieve a fill factor approaching 100% due to the issue of overlap and interstitial feature creation, such as in the case of the hierarchical arrays. This means that less light will be focused than with a completely packed square or hexagonal lens array. Second, the lenses presented above show an astigmatism which is evident in the discrepancy between the two measured focal

lengths in Table 6.2. We believe that this is caused by unintended lateral flow of the lens material due to slight variations among the spacer heights. This would mean that there was a slight tilt between the cooled window and the supporting substrate which leads to macroscopic lateral flow. Regardless, both of these issues could be resolved through further experimental and numerical studies of the fabrication parameters.

6.7 Summary

Thermocapillary sculpting with MicroAngelo has been shown to be a viable, single-step method of fabricating microlens arrays by projecting a temperature field onto a polymer surface using thermal conduction from photoresist patterns. A wide range of microlens topographies are available, controlled by a number of tunable process parameters. Feature overlap can be used to create highly nontrivial features, including hierarchical arrays and caldera-like arrays, in a single process step. The functionality of the fabricated MLAs has also been proven in a wavefront sensing application.